Journal of Solid State Chemistry 184 (2011) 44–51

Contents lists available at ScienceDirect

Journal of Solid State Chemistry

journal homepage: www.elsevier.com/locate/jssc

# $Na_{27}Ru_{14}O_{48}$: A new mixed-valence sodium ruthenate with magnetic heptameric plaquettes

J.M. Allred [a,*], L.M. Wang [b], P. Khalifah [b,c], R.J. Cava [a]

[a] Department of Chemistry, Princeton University, Princeton, NJ 08544, USA
[b] Brookhaven National Laboratory, Upton, NY 11973, USA
[c] Department of Chemistry, SUNY Stony Brook, Stony Brook, NY 11974, USA

ARTICLE INFO

*Article history:*
Received 20 July 2010
Received in revised form
7 October 2010
Accepted 12 October 2010
Available online 20 October 2010

*Keywords:*
Ruthenates
$Na_{27}Ru_{14}O_{48}$
Magnetic properties
Single crystal diffraction

ABSTRACT

$Na_{27}Ru_{14}O_{48}$ has been synthesized in air at 700 °C. The composition and crystal structure of the phase were determined by single crystal X-ray diffraction. The triclinic crystal structure contains isolated planar $Ru_7O_{24}$ plaquettes made from seven edge-sharing $RuO_6$ octahedra. The complex Na:Ru ratio is a result of tilting of the plaquettes to disrupt the packing of nominally hexagonal close packed planes made of Na ions and $RuO_6$ octrahedra. Resistivity measurements show that the material is semiconducting with an activation energy of 0.53 eV. The observed magnetic moment of 3.11 $\mu_B$ per Ru is lower than the expected spin only value, but is within the range seen in other compounds and is too large to indicate that the fundamental magnetic entities are the isolated $Ru_7O_{24}$ plaquettes. Small, reproducible deviations in the Curie–Weiss behavior occur below 200 K and the onset of a broad magnetic transition is seen between 40 and 32 K.



## 1. Introduction

Interest in the magnetic and electronic properties of ruthenium-based oxides is motivated by the fact that in spite of the presence of an abundance of unpaired *d* electrons, strong Ru–O covalency can lead to delocalized electronic states in some materials. Consequently complex electronic and magnetic properties are often found at the border between localized and itinerant behavior. Some ruthenates with unique properties are $Sr_2RuO_4$, an exotic low temperature superconductor [1], $SrRuO_3$, the 4*d*-based oxide ferromagnet with the highest $T_c$ [2], and $La_4Ru_6O_{19}$, a material that exhibits ferromagnetic quantum critical behavior [3]. To further expand this repertoire of properties, new materials are continually being sought. The sodium ruthenium oxide system specifically has seen a resurgence of interest in the last decade [4–11].

Sodium ruthenates are a fertile ground for interesting structures because the large alkali ions impose relatively lax restraints on their coordination polyhedra. This enables the transition metal atoms to order into features that would otherwise be excluded under the presence of a more rigid coordination condition on the other cations. This property accommodates the formation of interesting structures such as $Na_3MO_4$ ($M$=Nb, Ta, Ru) [12], where the $M^{5+}$ ions arrange themselves in isolated tetrameric plaquettes and the $Na^+$ ions fill intermediary distorted octahedral sites. The ruthenium variant has been of interest recently because it appears to be a low-dimensional magnetic "spin-lozenge" material [6,13]. The $Ru^{5+}$ ion is $4d^3$, and has been shown to display a local spin 3/2 moment that orders antiferromagnetically at 29 K [6,12,13]. Despite the isolated plaquettes, recent studies suggest that the long range ordering occurs through sufficiently strong interplaquette extended superexchange interactions [9,14,15].

While the synthesis of alkali ruthenates is challenging due to the volatility of alkali oxides, it would be fair to assume that after decades of work all of the compounds that could be synthesized in a straightforward fashion would have been discovered. Nonetheless, here we report the discovery of a new sodium ruthenate, $Na_{27}Ru_{14}O_{48}$, which can be synthesized using standard solid state procedures. Like $Na_3RuO_4$, $Na_{27}Ru_{14}O_{48}$ has isolated equilateral plaquettes made of edge-sharing $RuO_6$ octahedra (with seven rather than four octahedra per plaquette). This compounds has mixed valency, with the average Ru oxidation state slightly below five, and shows localized magnetic behavior, but with the spins displaying an effective moment smaller than the ideal $S$=3/2 per $Ru^{5+}$ ion. Evidence for a broad magnetic transition is seen in the magnetic susceptibility and specific heat between 32 and 40 K.

## 2. Experimental

### 2.1. Synthesis

Single crystals of $Na_{27}Ru_{14}O_{48}$ are obtained by heating pellets of intimately mixed $Na_2CO_3$ and $RuO_2$ (Alfa Aesar 99.5% and 99.999%,

* Corresponding author.
*E-mail addresses:* jallred@princeton.edu, jared.allred@gmail.com (J.M. Allred).

0022-4596/$ - see front matter © 2010 Elsevier Inc. All rights reserved.
doi:10.1016/j.jssc.2010.10.016

respectively), both dried, in an alumina crucible to 700 °C under air for three days. Crystals with nominally equivalent stoichiometry can be grown using a very wide range of input compositions, but approximately 10% excess sodium gives the best phase purity and crystal quality. Crystals are black and columnar with a metallic luster; dimensions are rarely larger than $0.4 \times 0.05 \times 0.05$ mm. The single crystals decompose slowly when exposed to moisture and dissolve readily in water and dilute mineral acids to produce an orange solution with a black precipitate that was confirmed by powder XRD to be $RuO_2$. All samples had some $RuO_2$ present as an impurity. Frequently, other impurities including $Na_3RuO_4$, $NaRuO_2$, $Na_xRuO_2 \cdot yH_2O$, and $Na_2RuO_4$ also occurred. Precise temperature control helped exclude these impurities but results were not always reproducible.

### 2.2. Single crystal X-ray diffraction

Diffraction data sets were collected on single crystals isolated from the reaction mixture using a Bruker Kappa Apex II single crystal X-ray diffractometer at 298 K with graphite-monochromated Mo $K\alpha$ radiation ($\lambda = 0.71073$ Å). Exposure time is 5 seconds/frame with detector distance at 70 mm. Unit cell refinement and data integration were performed with Bruker APEX2 software package. The crystal structure was determined using SHELXL-97 [16] implemented through WinGX [17]. X-ray powder diffraction collected on a Bruker D8-Focus with Cu-$K\alpha$ radiation was also used for characterization, though the reported crystal data is from the single crystal diffraction studies.

### 2.3. Physical properties

Physical properties were measured on a Quantum Design Physical Property Measurement System (PPMS). Unless otherwise noted, reported measurements are on pieces of polycrystalline pellet removed directly from the reaction mixture to minimize exposure to air. The crystals were too small for four-probe resistivity measurements, and thus only two-probe resistance was performed on a single crystal that was 0.4 mm long with a 0.01 $mm^2$ cross-section, using 13 μm gold wire adhered with silver paste. The high intrinsic resistance of the crystals, much larger than the contact resistance, made two probe resistivity measurements a viable procedure. Magnetic susceptibility measurements were performed on polycrystalline samples in applied fields of 50 kOe at temperatures between 2 and 300 K. The $M$ vs $H$ response was linear at all temperatures for fields up to the measurement field.

## 3. Results and discussion

### 3.1. Crystallographic refinement

Powder diffraction measurements of $Na_{27}Ru_{14}O_{48}$ (not shown) exhibit a very strong double peak at a $d$ spacing of ~9.1 Å, which cannot be ascribed to any previously reported sodium ruthenates. The diffraction data proved too complex to index the unit cell, so single crystals were taken for single crystal diffraction experiments. Most crystals checked for unit cell determination displayed either obvious signs of twinning or drastically streaked diffraction spots, which is indicative of stacking faults. Nevertheless, several crystals exhibited clean diffraction spots, and these were used for unit cell determination and structural refinement. Some angles in the reciprocal lattice are near 90°, but the deviation is statistically significant. The resulting triclinic cell is doubled by weak spots observed in the $bc$ plane. The latter cell was used for structural determination, and Table 1 shows the accompanying unit cell and final refinement data. The determined positional coordinates are reported in Table 2, and anisotropic parameters, which were refined for all atoms individually, can be found in the supporting information.

**Table 1**
Single crystal diffraction refinement data and parameters.

| **Crystal system** | Triclinic |
|---|---|
| **Space group** | $P$-1 (No. 2) |
| $a$ | 5.7763(4) Å |
| $b$ | 10.9910(9) Å |
| $c$ | 18.2042(13) Å |
| $\alpha$ | 88.517(4)° |
| $\beta$ | 87.194(3)° |
| $\gamma$ | 75.165(3)° |
| **Volume** | 1115.77(14) $Å^3$ |
| $Z$ | 1 |
| **Radiation wavelength** | 0.71073 Å |
| **Crystal size** | $0.211 \times 0.104 \times 0.055$ mm |
| **Absorption coefficient** | 4.988 $mm^{-1}$ |
| **Temperature** | 293(2) K |
| **2θ range** | 2.24–61.08° |
| **Resolution** | 0.4060 Å |
| **Scan mode** | $\omega$-scan+$\varphi$-scan |
| **F(000)** | 1297 |
| **Total reflections** | 6390 |
| **Reflections [$F_o > 4\sigma(F_o)$]** | 5302 |
| **Final $R$ indices [$F_o > 4\sigma(F_o)$]** | $R_1 = 0.0424$, $wR_2 = 0.1049$ |
| **Final $R$ indices (all reflections)** | $R_1 = 0.0539$, $wR_2 = 0.1101$ |
| $R_{int}$ | 0.0231 |
| $R_\sigma$ | 0.0418 |
| **G.O.F** | 1.054 |
| **Largest difference peak/deepest hole** | 2.551/−1.995 $e^-/Å^3$ |

However, without accommodating for crystallographic problems such as twinning or disorder, this refinement had problematic refinement parameters, $R_1 = 0.0600$ and $wR_2 = 0.1654$. The moderately large and irreducible refinement parameters were associated with four residual peaks near Ru5, Ru6, Ru7, and Ru8 with intensities between 8 and 11 $e^-/Å^3$. This is most likely indicative of lowered symmetry, crystallographic twinning, or disorder. To investigate lower symmetry, the data were also fit to a P1 unit cell, which yielded a structure that is indistinguishable from the $P$-1 model and with equivalent $R$ values, ruling out symmetry distortions. Twinning laws were sought both manually and by using computer software such as TwinRotMat [18] and ROTAX [19], yet no viable options were found, disqualifying twinning as a probable cause. To model disorder, first each sodium and ruthenium was checked for site splitting, but none were found. However, a disordered stacking fault model explains the spurious peaks. The perfect structure contains ABAB stacking; the stacking fault is modeled as randomly distributed layer mismatches, with some fraction of B layers becoming A, and vice versa. This is accomplished by treating the residual electron density in each layer as independent minor phases. The occupancy of sites in each minor phase should correspond to the relative fraction of faulted layers. Because the phase fraction was small enough only the ruthenium atoms can be distinguished from the noise with the exception of one extra sodium atom. Because an entire layer distorts at a time, distances between minor fraction and the major fraction are ignored.

The four largest residuals, located in the B layer, were set as ruthenium atoms Ru5′, Ru6′, Ru7′, and Ru8′. Four more residual peaks needed for this model were located near Ru2, Ru3, Ru4, and Na13 with peak heights between 3 and 5 $e^-/Å^3$. The first three of this set, Ru2′, Ru3′, and Ru4′, are located in the A layer, and the fourth, Na13′, is between layers. The site locations for these sites are listed for reference in Table 3, but the physical meaning of the sites should not be overstated. The model treated these eight atoms

**Table 2**
Atomic sites for $Na_{27}Ru_{14}O_{48}$ derived from single crystal X-ray diffraction. Sites used to model the stacking fault are not physically meaningful and are omitted from this table.

| Atom | Site | x | y | Z | $U_{iso}$*100 A$^2$ |
|---|---|---|---|---|---|
| Ru1 | 1*a* | 0 | 0 | 0 | 0.702(13) |
| Ru2 | 2*i* | −0.25365(9) | 0.23603(4) | −0.09699(3) | 0.818(11) |
| Ru3 | 2*i* | 0.02618(9) | 0.02984(4) | 0.17102(3) | 0.806(11) |
| Ru4 | 2*i* | −0.21674(8) | 0.26220(4) | 0.07410(3) | 0.792(11) |
| Ru5 | 1*g* | 0 | −1/2 | 1/2 | 1.182(15) |
| Ru6 | 2*i* | −0.14637(9) | −0.26813(5) | 0.39345(3) | 1.029(11) |
| Ru7 | 2*i* | 0.09866(9) | 0.46267(5) | 0.32944(3) | 0.927(11) |
| Ru8 | 2*i* | 0.27278(10) | 0.23148(5) | 0.43750(3) | 1.098(12) |
| Na1 | 2*i* | 0.1270(5) | 0.4065(3) | 0.15282(16) | 1.91(6) |
| Na2 | 2*i* | 0.1483(5) | 0.3656(3) | −0.04561(16) | 1.95(6) |
| Na3 | 2*i* | 0.2663(5) | −0.1996(3) | 0.27523(15) | 1.99(6) |
| Na4 | 2*i* | 0.3949(6) | 0.2027(3) | 0.24601(18) | 2.77(11) |
| Na5 | 2*i* | −0.4508(6) | 0.5089(3) | 0.18345(17) | 2.30(10) |
| Na6 | 2*i* | −0.3981(5) | −0.0728(3) | 0.15720(18) | 2.29(6) |
| Na7 | 2*i* | 0.1232(5) | 0.3149(3) | −0.22077(15) | 1.96(6) |
| Na8 | 2*i* | −0.0316(5) | 0.0888(3) | 0.33855(16) | 2.00(10) |
| Na9 | 2*i* | −0.6238(5) | 0.1408(3) | 0.05018(18) | 2.42(6) |
| Na10 | 2*i* | 0.1931(6) | −0.1156(3) | 0.49410(19) | 3.32(7) |
| Na11 | 2*i* | 0.5403(7) | −0.0204(3) | 0.3527(3) | 4.82(11) |
| Na12 | 2*i* | 0.4143(6) | −0.3739(3) | 0.4245(2) | 3.47(8) |
| Na13 | 2*i* | 0.6681(6) | 0.3682(3) | 0.3604(2) | 2.77(12) |
| Na14 | 1*e* | 1/2 | 1/2 | 0 | 4.56(16) |
| O1 | 2*i* | 0.0198(8) | −0.1506(4) | 0.1743(2) | 1.23(8) |
| O2 | 2*i* | −0.4520(8) | 0.2885(4) | −0.0057(2) | 1.10(8) |
| O3 | 2*i* | 0.1260(8) | −0.3609(4) | 0.3293(2) | 1.39(9) |
| O4 | 2*i* | −0.2191(7) | 0.0679(4) | 0.0839(2) | 0.85(8) |
| O5 | 2*i* | 0.0471(8) | 0.2014(4) | 0.1429(2) | 1.27(8) |
| O6 | 2*i* | 0.5628(9) | 0.1792(5) | 0.3873(3) | 2.28(11) |
| O7 | 2*i* | 0.0149(7) | 0.1813(4) | −0.0172(2) | 0.91(8) |
| O8 | 2*i* | 0.5846(9) | −0.2120(5) | 0.4660(3) | 2.10(10) |
| O9 | 2*i* | −0.1517(8) | 0.4189(4) | 0.0625(2) | 1.45(9) |
| O10 | 2*i* | −0.2587(7) | 0.0447(4) | −0.0764(2) | 0.91(8) |
| O11 | 2*i* | −0.5243(8) | 0.2705(4) | −0.1530(2) | 1.60(9) |
| O12 | 2*i* | 0.0771(9) | 0.2872(4) | 0.3508(2) | 1.49(9) |
| O13 | 2*i* | 0.0370(9) | −0.3248(4) | 0.4916(2) | 1.74(10) |
| O14 | 2*i* | 0.2825(8) | −0.5726(4) | 0.4312(2) | 1.49(9) |
| O15 | 2*i* | 0.2671(8) | 0.0110(4) | 0.2374(2) | 1.42(9) |
| O16 | 2*i* | 0.8224(8) | −0.4599(4) | 0.4101(2) | 1.42(9) |
| O17 | 2*i* | −0.1843(8) | 0.3893(4) | −0.1163(3) | 1.53(9) |
| O18 | 2*i* | 0.1911(10) | 0.0805(4) | 0.4401(3) | 2.00(10) |
| O19 | 2*i* | −0.2263(8) | 0.0667(4) | 0.2361(2) | 1.51(9) |
| O20 | 2*i* | −0.1188(10) | 0.4832(5) | 0.2573(3) | 2.17(11) |
| O21 | 2*i* | 0.6327(9) | −0.2351(5) | 0.3223(3) | 2.52(11) |
| O22 | 2*i* | −0.4672(9) | 0.3050(4) | 0.1394(3) | 1.82(10) |
| O23 | 2*i* | 0.3720(10) | 0.4140(5) | 0.2736(3) | 2.30(11) |
| O24 | 2*i* | −0.0462(9) | −0.1228(4) | 0.3861(3) | 1.91(10) |

**Table 3**
Atomic parameters used to model stacking faults.

| Atom | x | y | z |
|---|---|---|---|
| Ru2′ | −0.029(5) | 0.211(2) | −0.1051(14) |
| Ru3′ | −0.174(5) | 0.054(2) | 0.1660(14) |
| Ru4′ | −0.392(5) | 0.289(2) | 0.0171(8) |
| Ru5′ | −0.1205(22) | −0.4884(10) | 0.4970(5) |
| Ru6′ | −0.3413(17) | −0.2535(8) | 0.4017(5) |
| Ru7′ | −0.1232(17) | 0.4830(8) | 0.3280(5) |
| Ru8′ | 0.1207(18) | 0.2478(8) | 0.4255(5) |
| Na13′ | 0.763(5) | 0.289(2) | 0.2579(14) |

along with their associated major fraction counterparts as fractionally occupied, with each pair's occupancy constrained to sum to unity. All atoms within a layer individually refined to the same value within error, so each fraction had all members constrained to the same occupancy, which refined to 5.18(8)% and 1.71(8)% for the minor fractions in layers B and A, respectively. Na13 and Na13′ are unconstrained, but refine to 86.0(13)% and 10.23(12)%, which confirms that the sites are mutually exclusive. Each of the above revisions individually improve the refinement parameters, and together they give the final values reported in Table 1, which is a ~50% reduction in both $R_1$ and $wR_2$. $R_1$ is less than twice as large as $R_{int}$ and approximately equal to $R_\sigma$, which means that the fit has nearly reached the limit set by the quality of the data. The physical meaning of the stacking faults will be clarified in the ensuing structural discussion.

### 3.2. Structural discussion

The crystal structure is built from a repeating motif of isolated $Ru_7O_{24}$ plaquettes, shown in Fig. 1. These plaquettes consist of a single $RuO_6$ octahedron that shares edges with six other octahedra, forming a nearly regular planar hexagonal unit. No oxygen vertices are shared between neighboring plaquettes. The $Na^+$ ions are positioned between the plaquettes. Although a substructure with one $Ru_7O_{24}$ plaquette per cell can be defined, weak reflections in the single crystal data show that there are actually two unique plaquettes per unit cell, designated in the following as "plaquette A" and "plaquette B". These plaquettes are related but not identical. The central ruthenium atom of each plaquette lies on an inversion center, which means that there are only four crystallographically unique Ru atoms per plaquette. The dihedral angle between these four atoms is a metric for how close to a perfect plane each plaquette is; a dihedral angle of 0° is a perfect plane. In plaquette A this angle is 0.87(2)° and in plaquette B it is 3.36(2)°. The planes of the A and B plaquettes themselves are canted 16.6° with respect to each other, which is the distortion that gives rise to the doubled supercell.

The effect of the structural distortion is shown in Fig. 2. The so-called "ideal" sites were determined from a fit to the data to the 1/2 sized unit cell. Here the ideal sites of the sodium atoms are in the same planes as the plaquettes and extend the cationic triangular lattice defined by the ruthenium atoms. There are 15 such sodium sites per plaquette. However, due to the canting of the plaquettes, the sodium planes buckle slightly to accommodate the distortion. Part of the accommodation of this distortion involves the loss of three Na atoms per two plaquettes. Several models were tried for the sodium atom lattice. In the best and final structure there are 3 $Na^+$ ions missing from a regular hexagonal array per unit cell, which are excluded because the B plaquette canting disrupts the coordination of these sites. The surrounding $Na^+$ ions have moved toward the vacant positions to partially compensate for the missing ion. The data are fit poorly by models where the shifted neighboring sodium atoms are restored to more regular positions and the

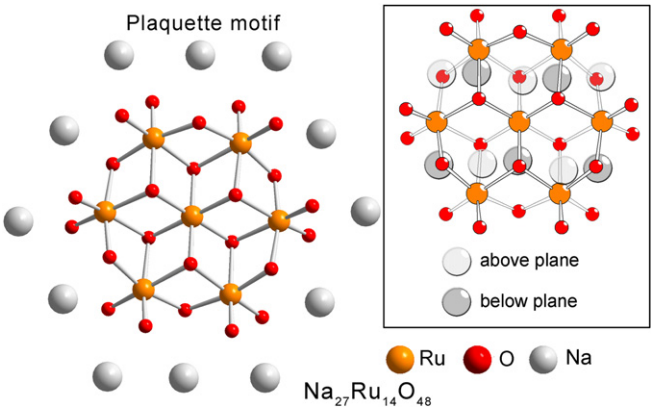


**Fig. 1.** Basic structural motif of $Ru_7O_{24}$ plaquette surrounded by sodium atoms. Atomic positions are taken from fit on simplified unit cell, so sites are idealized with respect to actual structure. Inset: There are five sodium sites both above and below the plaquette. Top and bottom are related by inversion symmetry.

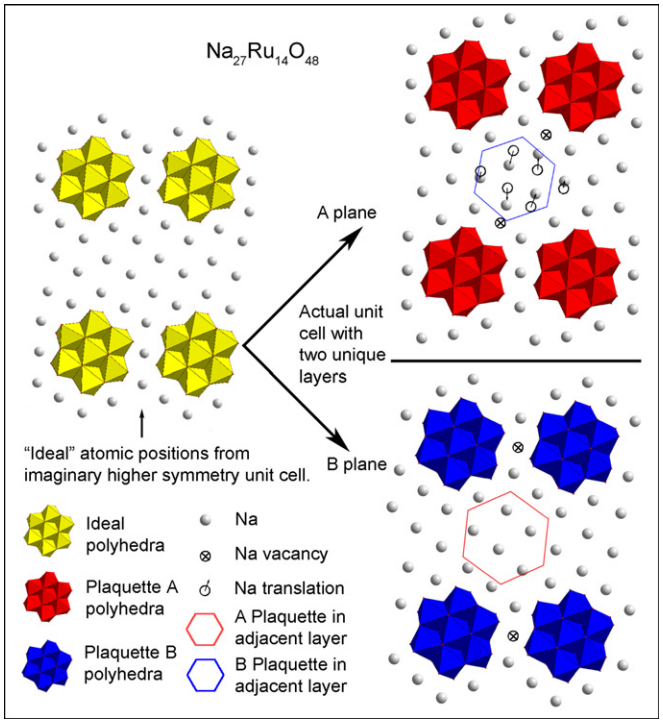


**Fig. 2.** Left: Idealized positions of atoms extended in the plane of the plaquette. Actual positions are shown for Planes A and B in middle and right panels, respectively. Crossed circles show vacancies and circles with arrows show lattice distortions from idealized positions. Hexagons depict the location of the B plaquettes above and below the A plane and vice versa.

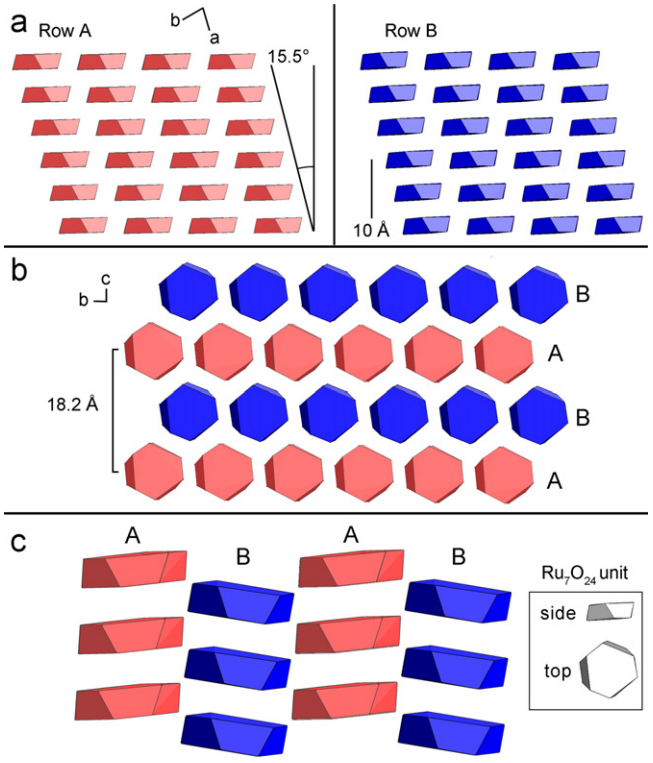


**Fig. 3.** (a) Projection of plaquettes in the plane of the rows (001 plane) with left panel: row A and right panel: row B. (b) Plaquettes viewed along the *a*-axis. (c) Rows A and B are staggered in the *a*-direction with respect to one another. Projection is in an arbitrary plane. Red (light) polyhedra represent the A plaquettes and blue (dark) polyhedra represent B plaquettes. (For interpretation of the references to color in this figure legend, the reader is referred to the web version of this article.)

vacancy is fractionally occupied. The structural model gives the final stoichiometry $Na_{27}Ru_{14}O_{48}$.

When thinking about the structure, it is productive to consider a sublattice defined by the plaquette positions. The central ruthenium atoms of all plaquettes lie in the *bc* plane, and are arranged in a pseudotriangular planar sublattice. This sublattice has translational vectors $b' = 10.510(19)$ and $c' = 10.754(19)$ Å and an angle of 117.76°, where the $b'c'$ and *bc* planes are equivalent. Thus the plaquettes lie in a nearly ideal triangular lattice. The stacking between these pseudotriangular planes corresponds to the *a* direction; the stacking of adjacent planes is only 4° sheared from an eclipsed geometry. The planes of the $Ru_7O_{14}$ plaquettes themselves, however, do not lie in the $b'c'$ pseudotriangular sublattice plane. Plaquettes A and B are tilted off this $b'c'$ plane by 32.1° and 31.8°, respectively.

While the above fully describes the arrangement of the lattice, an alternative way to rationalize the structure that considers the plaquettes as featureless regular hexagonal prismatic blocks can also be described. The $Na^+$ ions sit in interstitial sites on all sides of each hexagonal block and for the current purposes can be considered as part of the building blocks. The blocks stack perpendicular to their hexagonal faces with successive layers undergoing a moderate displacement (15.5° from the hexagonal block normal) from eclipsing directly. They thus form tilted columns, shown in Fig. 3a. In one direction the hexagons share an edge, forming rows. In each row, all of the plaquettes are crystallographically equivalent, so there are A and B rows formed from the respective plaquette. In Fig. 3a the left panel shows a segment of row A and the right panel shows row B. Neighboring rows are arranged in a staggered fashion to facilitate close packing (Fig. 3b), and occur in an ABAB arrangement. Finally, Fig. 3c shows how the vertical stacking is also staggered between rows, which further facilitates close packing. The usefulness of this description is that it clarifies that the structure is essentially a distorted hexagonally close packed array of plaquettes with much smaller sodium ions filling in the intermediary voids. This also explains the difficulty in determining the unit cell—the plaquette sublattices approximate a higher symmetry periodicity than is observed for the material as a whole.

The above structural description also allows an understanding of how stacking faults can occur in this structure. The largest residual peaks are in the B row, but the four peaks form a minor phase plaquette that shares three corners with the major phase plaquette. This minor phase is described within error by the same tilt angle as those observed in the major phase of plaquettes in row A. The only physical way that such a tilting can occur without tremendous strain is if the entire B row also tilts, which means that the disorder is really a stacking fault where ABABAB stacking becomes ABAAAB stacking ~5% of the time (based on the refined occupancies). Disorder on the A planes is less common based on Ru2′, Ru3′, and Ru4′, which refine to only ~1.5%. The very small occupancy means their positions are known less precisely making it difficult to precisely discern possible tilt angles in the A row minor phase. However, it is clear that A row faults do occur and that the tilt angle is closer to a B type plaquette than an A type plaquette. Finally, the last disordered atom is a sodium ion on the vacancy site shown in the A plane in Fig. 2. As described above, this is the site that cannot be filled due to the distortion effects from the tilting of plaquette B. This suggests that when there is an A–A or B–B interface this site is no longer vacant.

Taken together this suggests that the AB interface is the most energetically favorable, and a perfect crystal would have the stoichiometry $Na_{27}Ru_{14}O_{48}$. However, the strain in A–A interfaces is not large enough to completely exclude them, so entropy drives some fraction of B to A layer transformation. Apparently the B–B interface is even less favorable, so it only occurs rarely.

These imperfections also reduce the strain around an extra sodium atom located on the Na13′. This suggests that non-stoichiometry plays a role, although whether it is a driving force or not is unclear. The fact that Na13′ occupancy is higher than the incidence of stacking faults indicates that this is not a stringently enforced rule. Thus, it is not easy to determine the exact sodium content based on the refinement, but in this specimen it should be very close to $Na_{27}Ru_{14}O_{48}$.

The Ru–Ru nearest neighbor distances within the $Ru_7O_{14}$ plaquettes are all within 0.03 of 3.155 Å. The ruthenium ions in the six outer octahedra sit ~0.2 Å distally away from the octahedral centers. This distortion means that the outer ruthenium ions have 2 short, 2 medium, and 2 long Ru–O distances. These displacements from the octahedral centers indicate that coulombic repulsion is present. This is the primary interaction between the Ru cations; decreasing the coulomb repulsion is likely the driving force for the displacement of the outer Ru ions from the Ru in the central octahedron. Bond valence sums were calculated to build a picture of the approximate charge distribution within the plaquettes. The ionic valence, $V$, is a sum of the valences of each bond, $v_i$, and is calculated from bond length, $R_i$: $v_i = \exp\left(\frac{R_0 - R_i}{b}\right)$, where $R_0$ and $b$ are empirical constants (obtained from Ref. [20]) specific to particular ion pairs (e.g. $Ru^{3+}$ and $O^{2-}$). Thus, proper parameters must be chosen so that the calculations are self consistent. In an extended solid where the electrons may have itinerant character, the metallic valencies are not constrained to integer values. In these cases it is best to use $R_i$ values that agree best with the resulting $V$. Table 4 shows the results of this calculation, which are that the effective valencies of the Ru atoms in the central octahedron of plaquettes A and B are close to $3^+$ and $4^+$, respectively. The valencies for the Ru ions the outer octahedra are near $5^+$ for both plaquettes. Assignment of integer oxidation states of $3^+$, $4^+$, and $5^+$ to the Ru ions based on these calculations, which are not expected to be precise due to strain effects, yields a total charge that is very close to, but slightly lower than what is expected from the experimentally determined stoichiometry of the compound. The rational valencies obtained can be taken to indicate that to first order a localized picture of the electronic states in the Ru–O array can be considered as valid.

The bond valence sums indicate that the outer ruthenium sites in the plaquettes are all very nearly $Ru^{5+}$, whereas the central atoms in plaquettes A and B, Ru1 and Ru5, match more closely $Ru^{3+}$ and $Ru^{4+}$, respectively, indicating that the electron distribution on the Ru ions within the plaquettes is weighted towards the center. This can be understood as a stabilizing effect based on Pauling's electrostatic rules. The oxygen atoms in the central octahedron are coordinated to many high valence Ru atoms (3) and fewer $Na^+$ ions (usually 2); the oxygen atoms in the outer octahedra atoms have a greater number of $Na^+$ neighbors (3–5) and only 1 or 2 Ru neighbors. Thus, an extra electron or two on the central ruthenium will stabilize the coordination environment of those oxygen atoms by bringing the valence sum around them closer to 2+. Plaquette B's central oxygen atoms are together coordinated by one fewer $Na^+$ ion, which further substantiates the difference in calculated electron count between the two plaquettes. It also reaffirms the suggested correlation between stacking faults and non-stoichiometry of $Na^+$ ions.

**Table 4**
Calculated bond valence sums for ruthenium atoms in $Na_{27}Ru_{14}O_{48}$. The second column gives the valence used for $R_i$ that gave the best agreement between columns.

| Atom | Valence | $V$ | Average Ru–O bond distance (Å) |
|---|---|---|---|
| Ru1 | III | 3.09(6) | 2.017(5) |
| Ru2 | V | 4.92(7) | 1.991(5) |
| Ru3 | V | 5.03(7) | 1.9895(5) |
| Ru4 | V | 5.03(7) | 1.9895(6) |
| Ru5 | IV | 3.98(6) | 1.9867(6) |
| Ru6 | V | 5.07(8) | 1.9848(6) |
| Ru7 | V | 5.10(8) | 1.9842(6) |
| Ru8 | V | 4.98(7) | 1.9952(6) |

### 3.3. Resistivity

Single crystal resistance measurements (Fig. 4) show non-metallic behavior, with $dR/dT < 0$. The small crystal cross-section and high intrinsic resistivity did not allow for single crystal measurements to be made below 250 K. The large measured resistance means that contact resistance contributes negligibly to the total resistance, so the resistivity of the crystal can be calculated. The observed exponential relationship $\rho = \rho_0 e^{E_a/k_B T}$ is typical of semiconductors. Rearranging gives $\ln(\rho) = \frac{E_a}{k_B}(1/T) + \ln(\rho_0)$, where $E_a$, the thermal activation energy, is 0.533(2) eV. The very high resistivity is consistent with the expectation based on the crystal structure that the $Ru_7O_{14}$ plaquettes are electronically isolated from one another; little electron hopping between plaquettes is present.

### 3.4. Magnetism

The temperature dependent magnetic susceptibility, $\chi = M/H$, is plotted in Fig. 5. At temperatures higher than 40 K, the compound displays Curie–Weiss behavior, $1/\chi - \chi_0 = 1/C(T - \theta_W)$. Fitting to the high temperature (225–300 K) data only yields $\theta_W = -75.1(11)$ K, $C = 1.215(4)$ $mol_{Ru}$ Oe $emu^{-1}$ $K^{-1}$, and $\chi_0 = 0.0003$ emu $mol^{-1}$ $Oe^{-1}$. A subtle but reproducible feature is seen near 200 K that only negligibly alters the fit parameters, but a more dramatic feature, which must be due to the onset of a broad magnetic transition, is seen at 40 K. Between 25 and 40 K the magnetic susceptibility changes relatively little, and then on cooling below 25 K a small increase in magnetic susceptibility is observed. Based on a simple local electron picture, likely valid to a first approximation due to the isolated plaquettes and the poor conductivity of the compound, expected spin only moments are $S = 3/2$ for each $Ru^{5+}$ ion, $S = 1$ for each $Ru^{4+}$ ion, and $S = 1/2$ for each $Ru^{3+}$ ion. Considering the stoichiometry only, $Na_{27}Ru_{14}O_{48}$, 13 $Ru^{5+}$ and 1 $Ru^{4+}$ are expected, giving a spin-only $\mu_{eff} = 3.81$ $\mu_B$/Ru. Alternatively, considering the 7-Ru plaquettes and the bond valence sums, suggests that 12 $Ru^{5+}$, 1 $Ru^{3+}$, and 1 $Ru^{4+}$ are present. This scenario

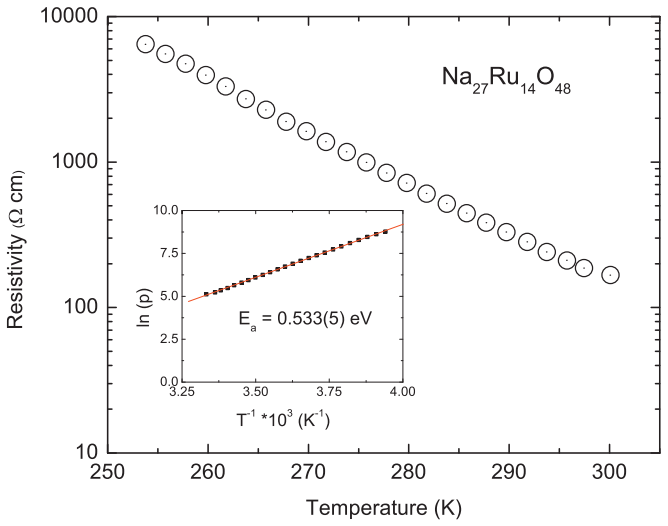


**Fig. 4.** Resistivity vs temperature on single crystal. Inset shows the linear behavior of $\ln(\rho)$ vs $T^{-1}$.

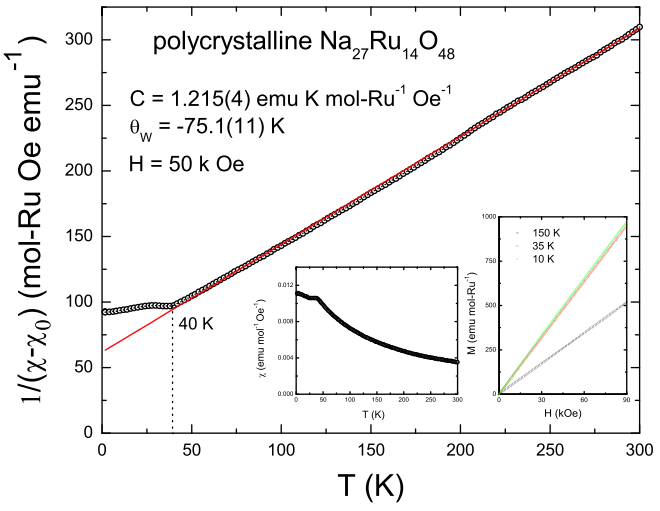


**Fig. 5.** (a) Magnetic susceptibility plotted as $1/(\chi-\chi_0)$ vs $T$ to show the subtle deviation from Curie–Weiss behavior below 200 K. Left inset: $\chi$ vs $T$. Right inset: $M$ vs $H$ at 150 K (black squares), 35 K (red circles), and 10 K (green triangles). (For interpretation of the references to color in this figure legend, the reader is referred to the web version of this article.)

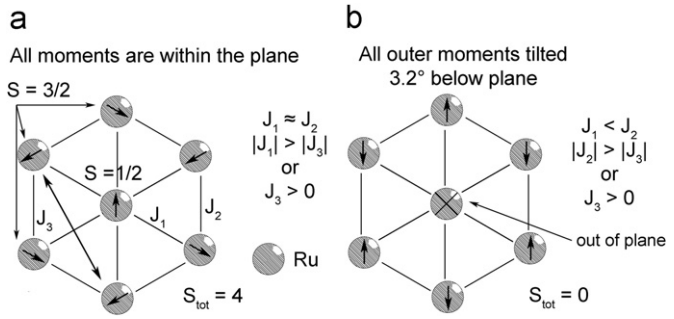


**Fig. 6.** Possible ground state for intraplaquette exchange interactions for (a) model based on 2D triangular Heisenberg lattice and (b) a possible ground state with zero net spin. Only ruthenium atoms are depicted for simplicity.

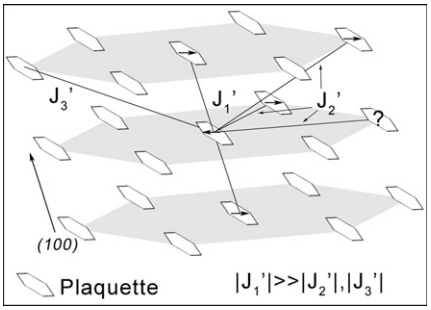


**Fig. 7.** Representation of geometric frustration in a simple model treating each plaquette as an isolated spin. Note that each hexagon represents an entire unit from Fig. 6.

would yield $\mu_{eff}=3.69\ \mu_B$/Ru from spin-only interactions. The measured effective magnetic moment ($\mu_{eff}$) per Ru is 3.11 $\mu_B$. While, this is smaller than the spin only value for both scenarios, it is within the typical range for the effective moment per $Ru^{5+}$, which varies greatly between compounds. For example, in $A_3BRuO_6$ materials, where $A$=Ca, Sr and $B$=Na, Li, there are isolated $Ru^{5+}$ ions in oxygen octahedra, and $\mu_{eff}$ ranges from 3.00 to 3.36 $\mu_B$/Ru[21]. The data fits within this range, and implies that most of the Ru 4*d* electrons contribute to the paramagnetism above 40 K.

The measured $\theta_W$ in this case shows that antiferromagnetic interactions among Ru atoms within the plaquettes dominate the magnetism. The peak in susceptibility at 40 K is indicative of some form of ordering, but the presence of a residual susceptibility below this temperature suggests that the ordering is atypical—the spins have not been fully paired at the magnetic transition. Ordinary antiferromagnets usually show a linear response to field strength in their magnetization below the ordering temperature, and this was indeed observed in $Na_{27}Ru_{14}O_{48}$ at the three temperatures measured: 150, 35, and 10 K.

The simplest model for the magnetic behavior of $Na_{27}Ru_{14}O_{48}$ would consist of short range ordering at higher temperatures due to intraplaqeutte interactions dominated by superexchange, followed by interplaquette ordering at lower temperatures due to weaker, less direct exchange interactions. Within the plaquettes, the ruthenium ions are arranged at the vertices of six edge sharing triangles, a geometrically frustrating geometry. Because the Ru ions form nearly equilateral triangles, it is reasonable to model the system with the most commonly found 2D triangular Heisenberg lattice analog [22] where the compromise ordering is a 120° arrangement of neighboring spins (Fig. 6a). However, unlike the infinite analog, the plaquette likely has residual spin in this analog due to incomplete cancellation of the local moments. This residual spin should be $S=4$ and 7/2 for plaquettes A and B, respectively, if a simple ordering scheme within the plaquette holds, but will be different if the finite size of the plaquette relaxes some of the magnetic frustration. If the observed magnetic susceptibility at high temperatures is due to the magnetic susceptibility arising from two magnetic plaquettes per cell, then the measured effective moment corresponds to $\mu_{eff}=11.67(2)\ \mu_B$/plaquette. This is somewhat larger than the 8–9 $\mu_B$ that is expected for the plaquettes based on the simple Heisenberg model. Since short range ordering within the plaquettes should yield a much lower value, this indicates that a model with short range magnetic ordering near room temperature is unlikely. The lack of metal–metal bonding at room temperature also is evidence against such a model.

Ordering within the plaquettes that does not extend to three dimensional interplaquette ordering would only result in a subtle feature in the susceptibility. This intraplaquette ordering may be what is observed near 200 K, but the significantly lower $\theta_W$(−75 K) argues against that explanation of the high temperature feature. Instead the intraplaquette magnetism may be manifested in the subtle deviations from Curie–Weiss behavior observed over the whole temperature range above 40 K.

How might long range antiferromagnetic ordering be achieved in $Na_{27}Ru_{14}O_{48}$? To do this, the residual spin in each plaquette must be completely canceled out through antialignment with the residual spin on neighboring plaquettes. We speculate that this can be accomplished by aligning the spins on plaquettes antiparallel to each other along *a*—the direction in which the plaquettes have the most facial overlap with each other. The separation between nearest neighbor plaquette (nnp) centers in this direction is ~5.8 Å. There are twelve next nearest neighbor plaquettes (nnnp), six in plane and six out of plane, which are all within 10.5–11.6 Å distance. There are another six plaquettes between 12.4 and 13.8 Å. This means that the interaction between the columns of nnp's along *a* reduces to another triangular lattice, also geometrically frustrated (Fig. 7). While the separations are apparently quite large, it must be remembered that the actual separations between plaquettes is the distance between neighboring oxygen atoms, which is near 3 Å for all neighbors.

Another model for ordering within the plaquette is possible if one assumes that the interaction between the center Ru and its neighbors ($J_1$) is weaker than the interactions between edge Ru atoms ($J_2$). In this case the system is no longer geometrically

frustrated, and the net spin can be completely canceled out in several ways. Fig. 6b shows one version, where the central spin is pointed directly out of plane. The moments on vertex Ru atoms need each only cant $\sim 3^{\circ}$ in the opposite direction to completely cancel this spin. Nevertheless, this model encounters many of the same problems finding a three dimensional ground state as the above model.

What is important for long range magnetic ordering is the strength and nature of the interplaquette Ru–O–O–Ru extended superexchange interactions. Such effects are generally considered weak or negligible, but in the case of $Na_3RuO_4$ they have been proposed as necessary to explain the long range ordering [15]. Without performing electronic calculations, what can be said is that nnp's have more extended superexchange interactions than the nnnp's do. This is likely more important than the apparent separation. It is also important to note that in spite of the frustrating geometries, a frustrating index ($|\theta_W/T_N|$) of $\sim 2$ is evidence against long-range magnetic frustration [22], though it is not known whether the susceptibility feature at 40 K represents long range magnetic ordering or not.

### 3.5. Heat capacity

The nature of the 40 K transition is potentially resolvable through measurement of the heat capacity through the same temperature regime. The heat capacity (Fig. 8) shows a broad feature significantly below the magnetic transition seen in the susceptibility. This feature appears in the $C_P$ vs $T$ plot as a minor bump, but in $C_P/T$ vs $T$ (Fig. 8 upper inset) it is clear that the bump is only a maximum in a feature that starts before 2 K and extends all the way up to at least 43 K. It has been shown[23] that for a simple antiferromagnet the behavior of zero field $\delta(\chi T)/\delta T$ and specific heat are similar near the ordering temperature. Usually the peak in $\delta(\chi T)/\delta T$ is a few Kelvin lower than the peak in $\chi$ and corresponds to the peak in specific heat, which is the case for this material where $\delta(\chi T)/\delta T$ (for $H=50$ kOe) occurs at 32 K (Fig. 8 lower inset).

Taken together with the magnetic data, the heat capacity supports the presence of short range magnetic ordering at $\sim 32$ K. As the system cools the onset of antiferromagnetic correlations become strongest around 40 K ($T_{\text{onset}}$). The entropy loss per Kelvin, defined by $\Delta S_{T_2 \to T_1} = \int_{T_1}^{T_1} \frac{C_P}{T} dT$, decreases until it is almost zero just before the second part of the transition ($T_N = 32$ K) where the excess entropy is then rapidly lost as the temperature continues to cool towards zero. The co-occurrence of a peak in both $C_P$ and $\delta(\chi T)/\delta T$ is a good basis for assigning this as the temperature of some type of magnetic transition. However, there is no sign of a $\lambda$-transition at $T_N$, which would be expected for ordinary antiferromagnetic ordering. Likely the transition is from a paramagnetic state above 40 K to a short range ordered state below 32 K, where the moments are ordered within the plaquettes but not long ranged ordered among plaquettes. The only minor increase in magnetic susceptibility below 32 K and the excess entropy observed in the specific heat suggest that there are significantly strong interplaquette interactions below $T_N$. It is also possible that this occurs because residual spins on plaquettes are freezing out or by interplaquette correlations such as long range magnetic ordering, perhaps along the (100) direction. Any real model for the behavior would need to take into account both superexchange and extended superexchange interactions between plaquettes. Specifically, the strength of interactions between interplaquette $Ru^{5+}$ atoms will have a strong effect on the magnetism. In addition to helping to understand the magnetism, such models may elucidate whether the structural distortion that creates the two independent $Ru_7O_{24}$ plaquettes is a result of packing effects or if it is electronic in origin.

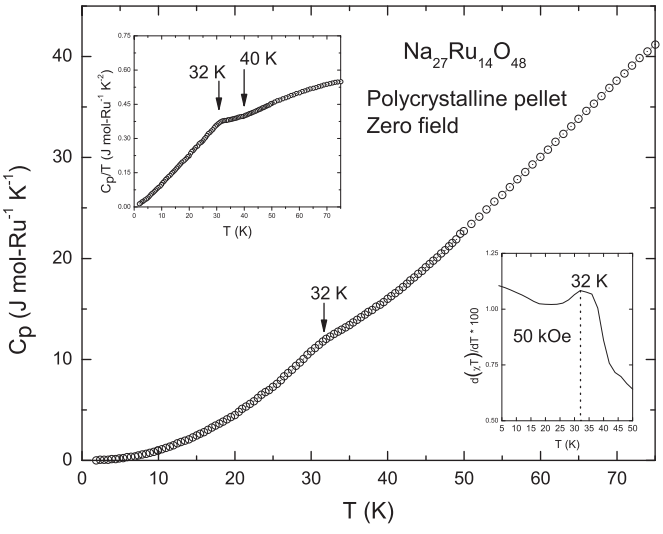


**Fig. 8.** Specific heat vs temperature on polycrystalline pellet. Arrows point to major feature. Inset top: $C_P/T$ vs $T$ with arrows pointing to important features in data. Inset bottom: $\delta(\chi T)/\delta T$ vs $T$ is nearly linear until critical point.

## 4. Conclusion

We have reported the synthesis and structure of $Na_{27}Ru_{14}O_{48}$. Our measurements have shown that the material has an electronic activation energy of approximately 0.5 eV and is very poorly conducting, indicating localized electronic behavior. Magnetically it displays somewhat less than the expected spin only $S=3/2$ per Ru ion, with some type of magnetic ordering below 40 K. The nature of the ordering is not yet well understood but is probably short ranged and may be described by geometrically frustrated plaquettes weakly coupled together as chains in the (100) direction. Further work on synthesizing larger crystals or polycrystals could allow for more precise measurements such as Mössbauer spectroscopy and powder neutron diffraction that would yield more insights into the nature of the magnetic state.

## Supporting information

Anisotropic thermal parameters and other relevant refinement data are found in the crystallographic information file (CIF) in the supporting information.

## Acknowledgments

J.M. Allred gratefully acknowledges helpful discussions with Dr. Shuang Jia, Dr. S.E. Dutton, and Prof. B.C. Chan. We would also like to thank J. Hanson for access to beamline X7B on the National Synchrotron Light Source at Brookhaven National Lab, where preliminary data sets were collected. This work was supported by the Solid State Chemistry program of the National Science Foundation, Grant NSF DMR-0703095.

## Appendix A. Supplementary materials

Supplementary data associated with this article can be found in the online version at doi:10.1016/j.jssc.2010.10.016.

## References


[1] G.M. Luke, Y. Fudamoto, K.M. Kojima, M.I. Larkin, J. Merrin, B. Nachumi, Y.J. Uemura, Y. Maeno, Z.Q. Mao, Y. Mori, H. Nakamura, M. Sigrist, Nature 394 (6693) (1998) 558–561.
[2] J.M. Longo, P.M. Raccah, J.B. Goodenough, J. Appl. Phys. 39 (2) (1968) 1327–1328.
[3] Y.A. Ying, K.D. Nelson, I.G. Deac, P. Schiffer, P. Khalifah, R.J. Cava, Y. Liu, Phys. Rev. B 80 (2) (2009).
[4] M. Shikano, R.K. Kremer, M. Ahrens, H.J. Koo, M.H. Whangbo, J. Darriet, Inorg. Chem. 43 (1) (2004) 5–7.
[5] M. Shikano, C. Delmas, J. Darriet, Inorg. Chem. 43 (4) (2004) 1214–1216.
[6] K.A. Regan, Q. Huang, R.J. Cava, J. Solid State Chem. 178 (6) (2005) 2104–2108.
[7] K.M. Mogare, D.V. Sheptyakov, R. Bircher, H.U. Gudel, M. Jansen, Eur. Phys. J. B 52 (3) (2006) 371–376.
[8] K.M. Mogare, K. Friese, W. Klein, M. Jansen, Z. Anorg. Allg. Chem. 630 (4) (2004) 547–552.
[9] J.T. Haraldsen, M.B. Stone, M.D. Lumsden, T. Barnes, R. Jin, J.W. Taylor, F. Fernandez-Alonso, J. Phys.: Condens. Matter 21 (2009) 50.
[10] R.V. Panin, N.R. Khasanova, A.M. Abakumov, W. Schnelle, J. Hadermann, E.V. Antipova, Russ. Chem. Bull. 55 (10) (2006) 1717–1722.
[11] K.A. Regan, Q. Huang, M. Lee, A.P. Ramirez, R.J. Cava, J. Solid State Chem. 179 (1) (2006) 195–204.
[12] J. Darriet, J. Galy, Bull. Soc. Fr. Mineral. Cristallogr. 97 (1) (1974) 3–5.
[13] M. Drillon, J. Darriet, R. Georges, J. Phys. Chem. Solids 38 (4) (1977) 411–418.
[14] T.C. Gibb, R. Greatrex, N.N. Greenwood, J. Solid State Chem. 31 (2) (1980) 153–169.
[15] F. Wu, E.J. Kan, M.H. Whangbo, Inorg. Chem. 49 (6) (2010) 3025–3028.
[16] G.M. Sheldrick, Acta Cryst. A64 (2008) 112–122.
[17] L.J. Farrugia, J. Appl. Cryst. 32 (1999) 837–838.
[18] A.L. Speck, J. Appl. Cryst. 36 (2003) 7–13.
[19] R.I. Cooper, R.O. Gould, S. Parsons, D. Watkin, J. Appl. Cryst. 35 (2002) 168–174.
[20] I.D. Brown, Accumulated Table of Bond Valence Parameters. 〈http://www.ccp14.ac.uk/ccp/web-mirrors/i_d_brown/bond_valence_param/bvparm2009.cif〉.
[21] J. Darriet, F. Grasset, P.D. Battle, Mater. Res. Bull. 32 (2) (1997) 139–150.
[22] M.F. Collins, O.A. Petrenko, Can. J. Phys. 75 (9) (1997) 605–655.
[23] M.E. Fisher, Philos. Mag. 7 (82) (1962) 1731–1743.